Research Article Vol. 30, No. 19 / 12 Sep 2022 / Optics Express 34172
Optics EXPRESS

Switchable ultra-broadband absorption and polarization conversion metastructure controlled by light

SIYUAN LIAO, JUNYANG SUI, AND HAIFENG ZHANG*

College of Electronic and Optical Engineering & College of Flexible Electronics (Future Technology), Nanjing University of Posts and Telecommunications, Nanjing 210023, China
*hanlor@163.com

Abstract: This article proposed a metastructure device that can realize polarization conversion (PC) and absorption function switching in the terahertz (THz) range based on the photoconductivity effect. The photoconductance is formed by exposing silicon to different intensities of light, then the PC and absorption function can be switched. At the same time, the absorption bandwidth is expanded by inserting air resonant cavities into the dielectric substrate, changing the thickness of the dielectric locally, and cutting rectangular slots at the metal bottom plate. When the device works as a polarization converter, linear-to-linear PC with a polarization conversion rate of over 90% at 0.96-1.47 THz can be achieved, and its relative bandwidth is 42%. And when the silicon conductivity is fixed at 3500 S/m through illuminating, the device switches to an ultra-broadband absorber with over 90% absorption at 0.75-1.73 THz and a relative bandwidth of 79%. The designed device can be applied efficiently in many fields, such as electromagnetic cloaking and communication.

1. Introduction

Metamaterial has been presented for decades as a new way to realize some effects that natural material cannot achieve, such as negative index of refraction [1], perfect absorber [2], and perfect lens [3]. With the development of metamaterial, this technology has been applied in many fields, including sensing, imaging, and communication [4–8]. Nowadays, metamaterial has developed from metasurface into metastructure, which comes from a two-dimensional structure to a three-dimensional one. The perfect metastructure absorber was first proposed by Landy *et al.* [9] in 2008, which realized perfect absorption in the microwave band through electric resonant rings and metal cut wires. With its ability to absorb nearly 100 percent of electromagnetic waves (EMW), the technology could have applications in the electronic stealth, light absorption, and electromagnetic pollution prevention and control. Among all kinds of absorbers proposed so far [10–13], there are ultra-broadband absorbers, tunable bandwidth absorbers, and photosensitive absorbers.

The metastructure polarization converters are also widely applied. With the development of communication technology, the traditional linear polarization antenna can not meet the needs of applications and has the disadvantages of poor anti-interference and high requirements for the direction of the incident wave. Therefore, the circularly polarized antenna is developed, but the traditional dielectric circularly polarized antenna also has the disadvantage of being difficult to integrate. Therefore, the polarization converters made of metastructures have irreplaceable advantages, including linear-to-linear polarization converters and circular-to-linear polarization converters which help linear polarization antenna work, linear-to-circle polarization converters used to generate circular polarization waves, and circular-to-circle polarization converters [14–18].

However, due to the complex working environment and the trend of integration, adjustable multifunctional devices have gradually become the development demand. There are various

#472336 https://doi.org/10.1364/OE.472336
Journal © 2022 Received 2 Aug 2022; revised 19 Aug 2022; accepted 24 Aug 2022; published 2 Sep 2022

Optics EXPRESS

ways to control devices, including but not limited to temperature [19], illumination [20], electric field [21], and gravity field [22]. Among them, active photonic materials that can be used for light control include liquid crystals [23], graphene [24], vanadium dioxide [19], silicon, etc. Among them, silicon, as a relatively traditional material, has the advantages of low cost, high quantum efficiency, and compatibility [25]. Moreover, the photoelectric effect of silicon is reflected in the enhancement of photoconductivity by the light-excited carriers, whose life is about several hundred nanoseconds, much longer than the picosecond time in the terahertz region. It is, therefore, possible to make devices that operate in the terahertz (THz) band by the silicon. For instance, in 2018, Song *et al.* [26] designed a THz absorber by taking advantage of changes in the conductivity of silicon, and in 2019, Zhao *et al*. [27] realized a tunable THz absorber using a single layer H-shaped all-silicon array. In 2021, Li *et al*. [28] realized the phase modulation of THz waves based on the silicon metastructure. Since there are few studies on the combination of absorber and polarization converter, in this paper, a photo-controlled multifunctional device with switching absorption and polarization conversion (PC) functions is proposed, which can switch functions by illumination control of silicon excitation in the device. On the other hand, to broaden the operating bandwidth of the device as an absorber, three steps are used to optimize the bandwidth which are inserting air resonators into the dielectric substrate, cutting rectangular slots on the metal bottom plate, and digging rectangular grooves at the top. With the help of these processes, when light shines on the device, stabilizing the conductivity σ of silicon around 3500 S/m, the device can achieve ultra-broadband absorption at 0.75-1.73 THz with absorptivity over 90%. Broadband linear-to-linear PC at 0.96-1.47 THz can be realized when there is no light and the conductivity of silicon is controlled near zero (σ =1 S/m). The relative bandwidths (RBs) of the absorber and PC are 79% and 42%, respectively.

2. Design processes and simulations

2.1. Structure and analysis of the initial device

The given device adopted a classic three layers structure, which consisted of a mixed pattern of silicon, and copper at the top, a dielectric layer, and a copper bottom plate. We choose polyimide with a dielectric constant of 3.5 [29] as the dielectric layer and use copper with conductivity at 5.8×10^7 S/m [30]. As displayed in Fig. 1(a), this model is called **structure 1**. When there is light, the part revealed in Fig. 1(b) works as a whole, and the silicon is excited to produce a photoconductor that can achieve the effects of an absorber. When there is no light, the silicon is not excited, only the copper arc can tailor EMW as presented in Fig. 1(c), and the given device can work as a polarization converter. When the device operates in an absorption state the conductivity of silicon is higher, when the impedance of the surface pattern matches the free space, the EMW can enter the device interior, which can produce current under the excitation of EMW. As a result, the magnetic resonance forms between silicon and copper plate and becomes the main way of EMW loss. When the device acts as a polarization converter, the copper arc completes the function of the PC. As demonstrated in Fig. 1(d), the copper arc is placed in a 45° direction, which means that when the incident EMW polarization along with the x or y direction. The produced current can be thought of as the sum of two components along u and v. The u-axis and v-axis are obtained by rotating the x-axis and y-axis 45° counterclockwise, and because the pattern performs different geometric characteristics in the u and v directions, thus, presenting different impedance to EMW, the reflected EMW will produce phase difference. When the phase difference equals 180°, the components in the v-direction will turn in the opposite direction $\boldsymbol{v}_-$, as the black arrow in Fig. 1(d) marks. At last, components along $\boldsymbol{u}$ and $\boldsymbol{v}_-$ compose the EMW along the x-direction.

As told above, the incident EMW $\boldsymbol{E_{in}}$ along the y-direction can be written as Eq. (1). And the reflected wave can be written in the matrix form of Eq. (2), where the r_{uv} and r_{vu} represent the cross-polarized reflection coefficients can be seen as 0 in theory, the co-polarized reflection

Optics EXPRESS

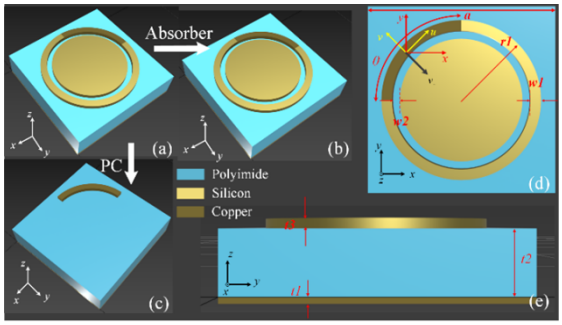

Fig. 1. (a) Schematic diagrams of the device, the blue part is polyimide, the bright yellow part is silicon, and the dark yellow represent copper. (b) and (c) show different part for absorption and PC respectively. (d) and (e) give the device size. $a = 144\,\mu m$, $r1 = 60\,\mu m$, $w1 = 8\,\mu m$, $w2 = 6\,\mu m$, $t1 = 3\,\mu m$, $t2 = 31\,\mu m$, $t3 = 5\,\mu m$, θ =90°.

coefficients r_{uv} and r_{vu} can be expressed as Eqs. (3) and (4). As a result, Eq. (2) can be simplified as Eq. (5).

$$\boldsymbol{E_{in}} = E_y\boldsymbol{i_y} = E_u\boldsymbol{i_u} + E_v\boldsymbol{i_v} \tag{1}$$

$$\boldsymbol{E_{ref}} = \begin{pmatrix} \boldsymbol{i_u} & \boldsymbol{i_v} \end{pmatrix} \begin{pmatrix} \boldsymbol{r_{uu}} & \boldsymbol{r_{uv}} \\ \boldsymbol{r_{vu}} & \boldsymbol{r_{vv}} \end{pmatrix} \begin{pmatrix} E_u \\ E_v \end{pmatrix} \tag{2}$$

$$\boldsymbol{r_{uu}} = |\boldsymbol{r_{uu}}|e^{j\phi_u} \tag{3}$$

$$\boldsymbol{r_{vv}} = |\boldsymbol{r_{vv}}|e^{j\phi_v} \tag{4}$$

$$\boldsymbol{E_{ref}} = \boldsymbol{i_u r_{uu}} E_u + \boldsymbol{i_v r_{vv}} E_v = E_y \cos(45°)(\boldsymbol{i_u r_{uu}} + \boldsymbol{i_v r_{vv}}) \tag{5}$$

It can be seen from Eq. (5) that if conditions (Eqs. (6) and (7)) can be satisfied, then the reflected wave can be further simplified into Eq. (8), the PC can be achieved.

$$|\boldsymbol{r_{uu}}| = |\boldsymbol{r_{vv}}| \tag{6}$$

$$\Delta\phi = \phi_v - \phi_u = \pi + 2k\pi, k \in Z \tag{7}$$

$$\boldsymbol{E_{ref}} = E_y \cos(45°)e^{j\phi_u}(\boldsymbol{i_u} + \boldsymbol{i_v}e^{j\Delta\phi})|\boldsymbol{r_{uu}}| = \boldsymbol{i_x}|\boldsymbol{r_{uu}}|e^{j\phi_u}E_y \tag{8}$$

The derivation above illustrates the generation of polarization transformation. What's more, the polarization conversion rate (PCR) can be used as an evaluation index to evaluate the performance of reflective polarization converters, as expressed in Eq. (9). PCR is generally required to reach more than 90%.

$$\mathrm{PCR} = \frac{{r_{xy}}^2}{{r_{xy}}^2 + {r_{yy}}^2} \tag{9}$$

In Eq. (9), r_{xy} and r_{yy} are the cross-polarized and the co-polarized reflection coefficients, respectively, and they can express as Eqs. (10) and (11). $\boldsymbol{E_{yi}}$ represents the electric field of incident wave polarized in the y-direction, $\boldsymbol{E_{yr}}$ and $\boldsymbol{E_{xr}}$ are the electric fields reflected which are polarized in the y- and x-directions, respectively. Therefore, the reflectivity (R) can be written as Eq. (12).

$$r_{xy} = |\boldsymbol{E_{xr}}|/|\boldsymbol{E_{yi}}| \tag{10}$$

$$r_{yy} = |\boldsymbol{E_{yr}}|/|\boldsymbol{E_{yi}}| \tag{11}$$

$$R = |r_{xy}|^2 + |r_{yy}|^2 \tag{12}$$

When the device operates in absorption state, the absorption rate can be calculated according to Eq. (13), where T is the transmissivity and can be regarded as 0 for reflective devices. Thus,

Optics EXPRESS

the absorptivity can be simplified to Eq. (14).

$$A = 1 - R - T \tag{13}$$

$$A = 1 - R = 1 - |r_{xy}|^2 - |r_{xy}|^2 \tag{14}$$

The obtained results in Figs. 2(a) and 2(b) told that when the conductivity of silicon is fixed at σ=3500 S/m, two absorption peaks appear at 0.7 (0.61~0.86) THz and 1.38 (1.35~1.40) THz with absorptivity over 90%, and the minimum absorptivity between two peaks is more than 70%, which means a potential performance. The RB of the left narrow area is 34% and the right region is 3.6%. And when σ=1 S/m, there emerges a PC over 90% peak at 0.88 THz with a narrow band from 0.83 to 0.96 THz, and the RB is 18%. As can be seen from Fig. 2(c), there is no problem regarding transmittance as 0. Figure 2(d) is the curve of the phase difference, the calculation formula is Eq. (7), it can be verified from Fig. 2(d) that the phase condition is established at 0.88 THz, so, the PCR is close to 100% and is only generated at 0.88 THz, and as the phase gradually deviates −180° and PCR also decreased.

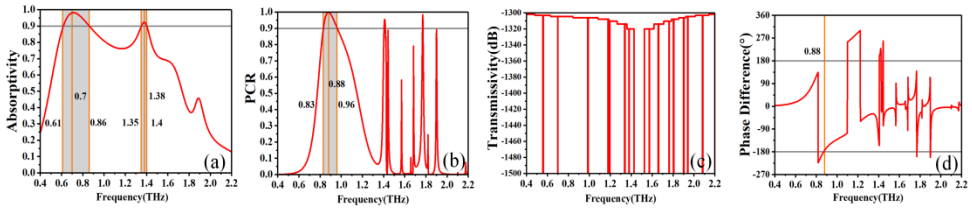

Fig. 2. (a) Absorptivity curve, conductivity of silicon: σ=3500 S/m, (b) PCR, σ=1 S/m, (c) transmissivity curve, (d) phase difference curve.

Through the current diagrams, we can clarify the reasons for the absorption and PC. As illustrated in Figs. 3(a) and 3(b). At 0.7 THz, the currents are concentrated under the silicon wafer. At 1.38 THz, the currents are focusing between period structures, which means the loss of EMW is caused by the resonance between period structures instead of a single element. And in the PC state, as indicated in Figs. 3(c) and 3(d), the current $\boldsymbol{I_1}$ on the upper copper arc and the current $\boldsymbol{I_2}$ on the bottom plate are opposite, so according to the right-hand rule, the upper and lower opposite currents generate magnetic moments and induce a magnetic field $\boldsymbol{H}$. According to the relationship between the electric field and the magnetic field, the process of PC can be described as follows: the component $\boldsymbol{H_y}$ of $\boldsymbol{H}$ in the y-direction will generate an electric field in the x-direction, which is an important reason for the PC. As can be seen from Fig. 3(d), the electric field along the positive direction of the y-axis should generate a magnetic field $\boldsymbol{H'_x}$ along the negative direction of the x-axis, which is opposite to the component $\boldsymbol{H_x}$ of $\boldsymbol{H}$ in the x-direction. The PC in the x-direction is completed.

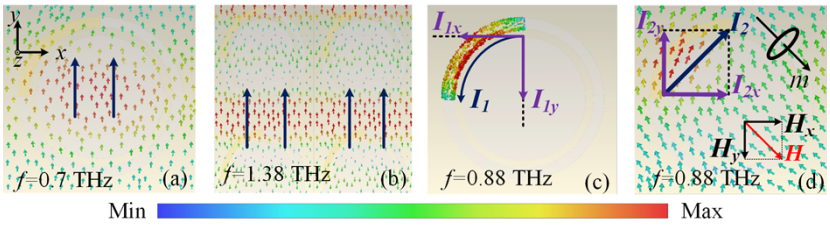

Fig. 3. (a) Absorption state, current at 0.7 THz. (b) Absorption state, current at 1.38 THz. (c) PC state, current on the copper arc. (d) PC state, current on the copper plate.

Optics EXPRESS

2.2. Improve performance by slitting and double arcs

According to the results in Section 2.1, the disadvantage of this metastructure is that the working area is too narrow. So, the next step is to broaden the absorption and PC band. The improved structure is demonstrated in Figs. 4(a)-(c) and the parameters are given in Figs. 4(d) and 4(e). To improve the bandwidth, the silicon wafer is cut with concentric rings, and an arc at the symmetrical position of the copper arc is added. This operation can add a new resonance mode between different parts of the silicon wafer and the initial resonance mode will not be broken. In the PC state, this operation increases the density of arcs, it is the reason why the PC band is broadened. This model is called **structure 2**.

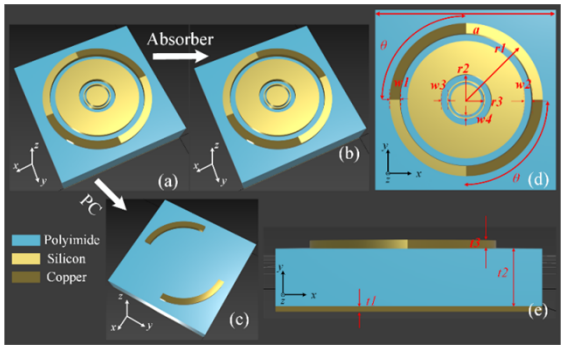

Fig. 4. (a) The schematic diagrams of device with slit on silicon wafer and double arcs. (b) and (c) different parts for absorption and PC. (d) and (c) show the detailed parameters. $a = 144\,\mu m$, $r1 = 60\,\mu m$, $r2 = 20\,\mu m$, $r3 = 14\,\mu m$, $w1 = 8\,\mu m$, $w2 = 6\,\mu m$, $w3 = 5\,\mu m$, $w4 = 2\,\mu m$, $t1 = 3\,\mu m$, $t2 = 31\,\mu m$, $t3 = 5\,\mu m$, θ =90°.

In Figs. 5(a) and 5(b), it can be seen that a comparison of the performance of **structure 1** and **structure 2**. The low-frequency part of the absorptivity curve is decreased while the high-frequency part is increased, and the overall absorptivity indicates an upward trend. The lowest absorption rate increases from below 75% to more than 80%, and the absorption peaks appear at 0.65 and 1.37 THz. The right peak gets to more than 90% during 1.31~1.40 THz, and the RB is 6.6%. For PCR, compared with the single-arc structure, the bandwidth of the double-arc structure is significantly wider. The available bandwidth ranges from 0.74 to 1.36 THz, and the RB is 59%. It can be seen from Fig. 5(c) that after adding an arc, the phase difference of the originally relatively flat but unsatisfactory part is reduced to 180 degrees, which is the reason for the expansion of the PCR bandwidth.

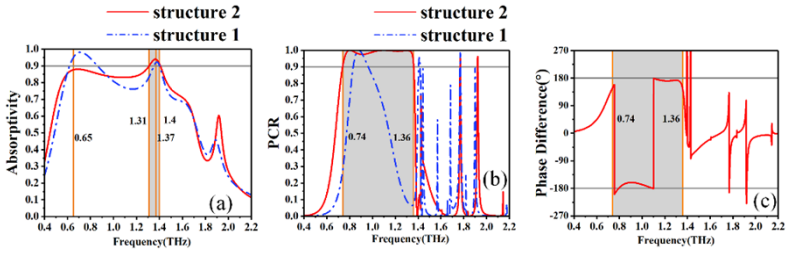

Fig. 5. (a) The curves of absorptivity (conductivity of silicon: σ=3500 S/m). (b) PCR curves (σ=1 S/m). (c) The curve of phase difference.

Optics EXPRESS

2.3. To improve performance by inserting air resonance cavities

By the step mentioned above, we successfully widen the operating band of the PC. But it still needs improvement that 80% absorptivity is not satisfied. So, as displayed in Fig. 6(a), the changed model is called **structure 3**, and some cavities are added into polyimide, the dielectric substrate. Those cavities are consisted of two shapes, as illustrated in Figs. 6(e) and 6(f), one of them is a frustum of a cone, whose radius of top surface *R1* is smaller than the radius of bottom *R2*, and the other kind, that the radius of top surface *R1* is bigger than the radius of bottom *R3*. Except for the cavities, the other parts are the same as **structure 2**.

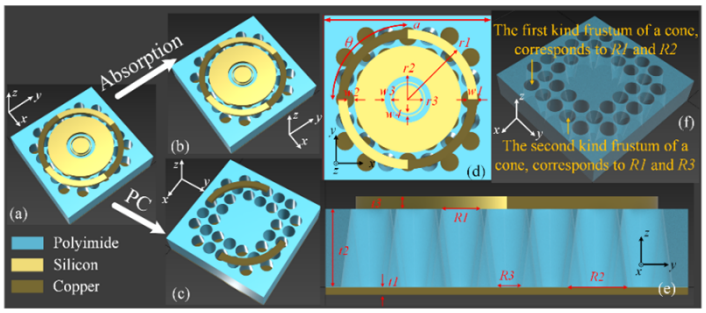

Fig. 6. (a) The schematic diagram of structure 3. (b)-(c) The different parts for absorption and PC. (d)-(e) The parameters of device. (f) The perspective view to explain how the two kinds of inserted cavities look like. $a = 144\,\mu m$, $r1 = 60\,\mu m$, $r2 = 20\,\mu m$, $r3 = 14\,\mu m$, $w1 = 8\,\mu m$, $w2 = 6\,\mu m$, $w3 = 5\,\mu m$, $w4 = 2\,\mu m$, $t1 = 3\,\mu m$, $t2 = 31\,\mu m$, $t3 = 5\,\mu m$, $R1 = 16\,\mu m$, $R2 = 24\,\mu m$, $R3 = 8\,\mu m$, $\theta = 90°$.

In Figs. 7(a) and 7(b), which reveal the absorptivity and PCR of **structure 3**, it could be figured out that the absorptivity measures up 90% between 0.75 and 1.64THz under the help of cavities, resulting in a bandwidth of 0.89 and a RB of 74%. It indicates the effects of cavities that form resonate cavities to enhance the loss of EMW. As a result, the working area is widened and absorptivity is increased. To the PCR, the cavities can slightly broaden bandwidth to 0.62 THz from 0.87 THz to 1.49 THz, and the PCR within the working zone mostly achieves 99% and the RB is 69%. What's more, both the absorber and PC band are moved to a higher frequency, which is caused by cavities. Correspondingly, the phase curve also shifts towards higher frequencies.

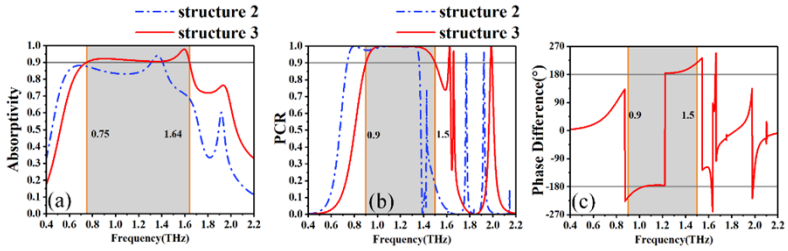

Fig. 7. (a) Absorptivity, form operating range of 0.75-1.64 THz, working bandwidth is 0.89 THz. (b) Improved PCR, with working bandwidth reaches 0.6 THz in the range of 0.9-1.5 THz. (c) Phase difference in PC state.

2.4. Improve performance by slitting rectangular slots on substrate

As mentioned above, the absorption of the high-frequency part mainly depends on the resonance between the cells, which is not the same as the current position of the low-frequency part.

Optics EXPRESS

Therefore, to further improve the performance of the device, changing the current path by cutting rectangular slots on the base plate is a feasible method. The new model (**structure 4**) is signified in Figs. 8(a)-(f). The difference from **Structure 3** is that L-shaped slots are added to the metal bottom plate. Figure 8(g) is a partially enlarged view of Fig. 8(f), the dimensions *L1*, *L2*, and the width *w5* of the two slots are given.

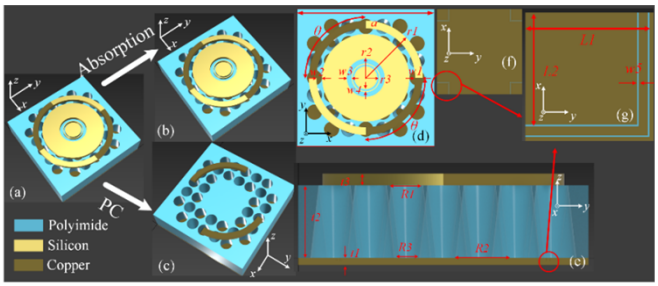

Fig. 8. (a) The schematic diagram of device slitting seams on bottom. (b)-(c) different parts for absorption and PC. (d),(e) the structural parameters of device. (f) the back view of device, show the locate of four groups slots. (g) enlarged view of thin slots on substrate and size of the slots. $a = 144\,\mu m$, $r1 = 60\,\mu m$, $r2 = 20\,\mu m$, $r3 = 14\,\mu m$, $w1 = 8\,\mu m$, $w2 = 6\,\mu m$, $w3 = 5\,\mu m$, $w4 = 2\,\mu m$, $w5 = 0.25\,\mu m$, $t1 = 3\,\mu m$, $t2 = 31\,\mu m$, $t3 = 5\,\mu m$, $R1 = 16\,\mu m$, $R2 = 24\,\mu m$, $R3 = 8\,\mu m$, $L1 = 21\,\mu m$, $L2 = 19.2\,\mu m$, $\theta = 90°$.

As can be seen in Fig. 9(a), the peak at 1.6THz that appears in the original **structure 3** has become flat. Meanwhile, the bandwidth attains 0.94 THz at 0.74-1.68 THz. Although this change is slight, it can change the resonating between period structures at the corners. In addition, in Fig. 9(a), the loss of PC state is also marked with a green dash line, and a sharp absorption peak appears at 1.68 THz. In Fig. 9(b), PCR is given, the working region is 0.9-1.5 THz, and the bandwidth is 0.6 THz, so, the new absorption peak will not affect the PC effect. The PCR of **structures 3 and 4** in the working region is indistinguishable. The RB as an absorber is 77%, and the RB as a polarization converter is 50% Therefore, the main effect of slots on the substrate is successfully changing the resonance mode. The phase difference of the working region does not change significantly.

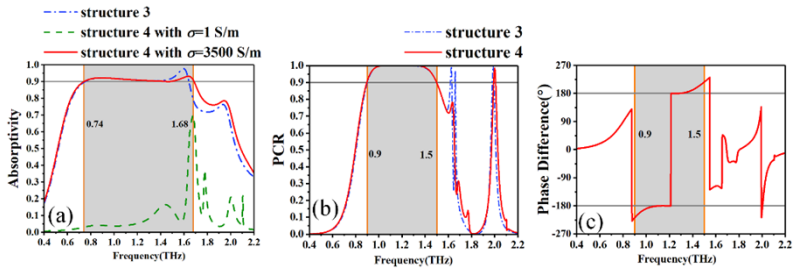

Fig. 9. (a) Absorptivity for both absorption and PC state. (b) The PCR of structures 4 and 3. (c) Phase difference in PC state.

2.5. *Improve performance by slotting grooves on the top surface of the dielectric*

According to Smith's work [31], the *S*-parameters are related to the thickness of the dielectric, as referred to in Eqs. (15) and (16). On the other hand, the place where high frequency resonates is different from low and middle frequency, that the former is between elements and the latter

Optics EXPRESS

is under silicon wafer (as mentioned in Fig. 3). Therefore, it is feasible that locally change the thickness of polyimide to match different frequencies at different places. Figure 10(i) reveals the array diagram during operation and Figs. 10(j) and 10(k) illustrate the definition of polarization angle and incident angle.

$$S_{21} = S_{12} = \frac{1}{\cos(nkd) - \frac{1}{2}(z + \frac{1}{z})\sin(nkd)} \tag{15}$$

$$S_{11} = S_{22} = \frac{i}{2}(\frac{1}{z} - z)\sin(nkd)S_{12} \tag{16}$$

$$A = 1 - R = 1 - |S_{11}|^2 - |S_{21}|^2 \tag{17}$$

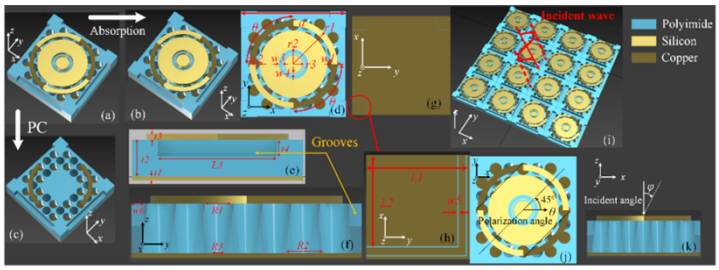

Fig. 10. (a) The schematic diagram of device slotting grooves on dielectric. (b)-(c) the different parts for absorption and PC. (d)-(h) the structural parameters of device. (i) the array arrangement of the given structure. (j)-(k) the polarization angle and incident angle of the device during operation. $a = 144$ µm, $r1 = 60$ µm, $r2 = 20$ µm, $r3 = 14$ µm, $w1 = 8$ µm,$w2 = 6$ µm, $w3 = 5$ µm, $w4 = 2$ µm, $w5 = 0.25$ µm, $w6 = 8$ µm, $t1 = 3$ µm, $t2 = 31$ µm, $t3 = 5$ µm, $t4 = 14$ µm, $R1 = 16$ µm, $R2 = 24$ µm, $R3 = 8$ µm, $L1 = 21$ µm, $L2 = 19.2$ µm, $L3 = 100$ µm, θ =90°.

In Fig. 10(a), four grooves are set at the edges of the dielectric, with the structural parameters *L3, t4*, and *w6*, as displayed in Figs. 10(e) and 10(f). This model is called **structure 5**. As a result, at the place corresponding to the high-frequency region, the thickness becomes thinner. Other parameters are not changed. Figs. 11(a) and 11(b) show the absorptivity and PCR curve of the device. In the diagram, the absorption bandwidth attains 90% at 0.75-1.73 THz with a width of 0.98 THz, and the RB is 79%. An absorption peak appeared again at 1.7 THz, which means that the thinner dielectric strengthens the loss in polyimide at a high frequency. Then, in Fig. 11(b), the working bandwidth of the PC is 0.51 THz at 0.96-1.47 THz with a RB of 42%, which is slightly shorter than the previous version. But compared with the increase in absorptivity, the loss in PCR is acceptable. In addition, the absorption peak in the PC state at 1.71 THz will not affect the operating zone either.

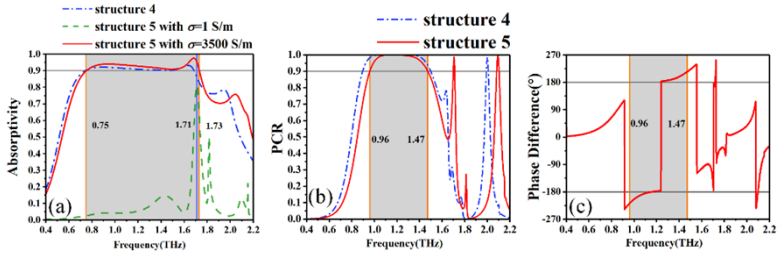

Fig. 11. (a) Absorptivity for both absorption and PC states, absorption peak in PC state is marked in blue line at 1.71 THz. (b) PCR. (c) Phase difference in PC state.

Optics EXPRESS

3. Result and discussion

The final design version which can realize a 0.98 THz absorption bandwidth and a 0.51 THz PC bandwidth is got in Section 2.5. In the absorption state, the working range is from 0.75 to 1.73 THz with absorptivity over 90%, and more than 79% RB. And in the PC state, the working region is from 0.96 to 1.47 THz with PCR over 90%, mostly over 99%, with 42% RB. The absorptivity and PCR of five structures in Section 2 are summarized in Fig. 12. Table 1 gives the position, absolute bandwidth, and the RB of the operating band of each structure. In the table, the two bandwidths of **structure 1** are the absorption peaks at low and high frequencies, respectively. The bandwidth of **structure 2** is reduced because the overall absorptivity is increased, but the part that achieved more than 90% decreased. It can be concluded from Table 1 that in terms of the bandwidth balance between the absorption state and the PC state, **structure 4** performs the best. However, to obtain a better absorption bandwidth, **structure 5** is a better choice. To demonstrate the advantages of this structure, we compare the recently published papers and list their performance in Table 2. It can be seen that the devices proposed in many papers have excellent performance, but the devices proposed in this paper also have irreplaceable characteristics.

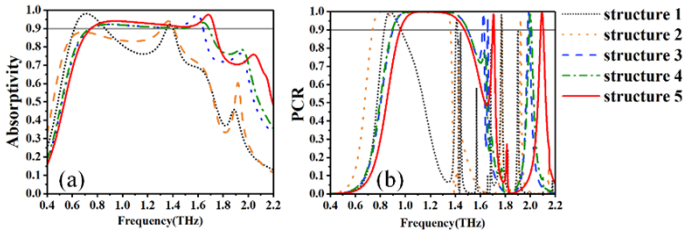

Fig. 12. The curve of structure 1-5. (a) absorptivity. (b) PCR.

Table 1. The performance of each structure

Performance \ Structures		1	2	3	4	5
Operating band (THz)	Absorption	0.61~0.86, 1.35~1.40	1.31~1.4	0.75~1.64	0.74~1.68	0.75~1.73
	PC	0.83~0.96	0.74~1.36	0.9~1.5	0.9~1.5	0.96~1.47
Absolute bandwidth (THz)	Absorption	0.25 0.05	0.09	0.89	0.94	0.98
	PC	0.16	0.62	0.6	0.6	0.51
RB (THz)	Absorption	34% 3.6%	6.6%	74%	77%	79%
	PC	18%	59%	50%	50%	42%

Table 2. The performance of each structure

References	[32]	[33]	[34]
Function	Absorption	Absorption PC	Absorption
Frequency (THz)	0.72~1.26	2.17~4.94 3.5~6	6.45~14.89
RB	54.5%	77.8% 52.6%	79%

Optics EXPRESS

3.1. Mechanism of physics

As can be seen from Figs. 13(a) and 13(b), the step of cutting concentric rings used in Section 2.2 generates resonance between the different rings, enhancing the current in the middle frequency (1.18 THz), which is the main reason for the improved absorptivity. Secondly, it can be found in Figs. 13(c), 13(d), and 13(e) that the current in the circle is significantly weaker in structure 4 than in structure 3, which suggests that the slots in the bottom plate in Section 2.4 actually changed the current at the center of the four units. As the current paths are forcibly blocked by the slots, the current in the rectangular slit is greatly weakened, so the resonance mode is changed and the absorption bandwidth is extended to a higher frequency. Thirdly, it can be seen from Figs. 13(f) and 13(g) that the step of locally thinning the dielectric mentioned in Section 2.5 effectively enhances the resonance between units and significantly enhances the current. This is because the absorption at the high frequencies is caused by the resonance between the elements, and the EMWs at the high frequencies match the thinner dielectric. On the other hand, in structure 5, the bandwidth of PC is reduced because the change of dielectric thickness affects the current on the backplane, and the PC depends on the magnetic resonance of the backplane current and the current on the arc.

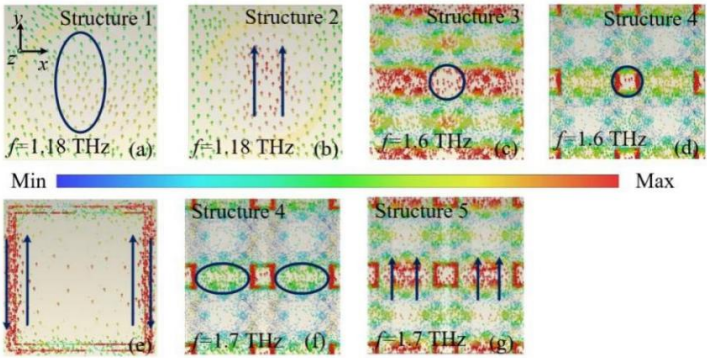

Fig. 13. The current contrast diagrams, (a)-(b) difference in current without and with the slots on the silicon wafer. (c)-(d) difference in current without and with the slots on the bottom. (e) the partial enlargement of the circled part in (d). (f)-(g) difference in current without and with the grooves on the top.

Regarding the step of adding air resonant cavities to the dielectric layer mentioned in Section 2.3, it is more suitable to use the electric energy density diagram to illustrate. Firstly, by comparing the top view of the electric energy density (Figs. 14(a)-(d)), it can be seen that before and after adding the air resonator, the energy density is significantly enhanced at the position circled in red in the diagrams. Secondly, it can be seen from the side view that the air column has an obvious confinement effect on the electric field. In Fig. 14(e), the energy is confined between the air column and the uppermost slit, and it is more obvious in Fig. 14(f). The air column constraining the energy under the silicon wafer increases the energy loss in the medium to achieve the effect of enhanced absorption. At the same time, since the resonator has the lowest resonant frequency, and there is no resonator under the silicon wafer, this creates a photon localized effect that changes the equivalent refractive index. This phenomenon is more pronounced at high frequencies, so the operating area appears to shift towards high frequencies after adding a resonator. The curves of rxy and ryy are demonstrated in Fig. 15. It can be seen that the reason why PCR moves to high frequency is that both rxy and ryy move to high frequency.

Optics EXPRESS

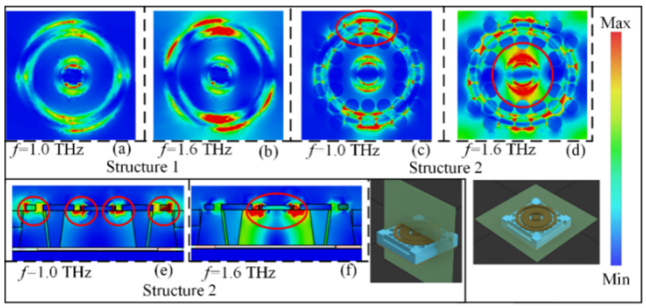

Fig. 14. The electric energy density diagrams for different structures at 1.0 and 1.6 THz. (a)-(d) The top views of structures 1 and 2. (e)-(f) The side view of structure 2.

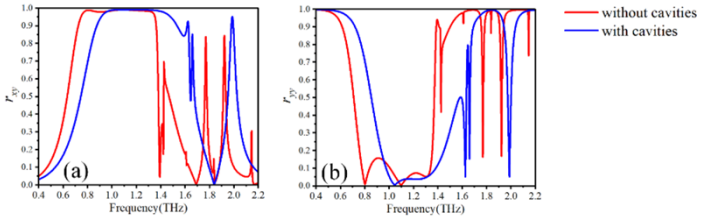

Fig. 15. (a) r_{xy} before and after adding air column (b) r_{yy} before and after adding air column.

3.2. *Influences of parameters*

During the process of optimization, there have found three important variables that the performance is sensible to value change of them: S, the conductivity of silicon; a, the length of a single element; $t2$, the thickness of polyimide. And other parameters are relative insensitivity that a small difference cannot produce an obvious change. Since the parameter σ involves the switching of the two states, the data from 0 to 4500 S/m is calculated for the absorption effect, as demonstrated in Fig. 16(a), and it can be seen that when σ is greater than 1000 S/m, the absorption bandwidth starts to increase significantly, so it can be considered that at σ=1000 S/m is the boundary between the two states. Starting from σ=3500 S/m, the bandwidth becomes stable, and when σ is greater than 4000 S/m, defects appear in the middle of the working area, so it is reasonable to set the working value of the absorber to σ=3500 S/m. Figure 16(b) reveals the PCR with σ from 0 to 1000 S/m, and it can be seen that the bandwidth of PCR is very stable. The parameter a is the side length of a single element, and the change of a will affect the resonance between the elements. Figure 16(c) evidences the change of the absorption bandwidth with a. It can be found that when a is less than 142 μm, the absorption area of the low-frequency part is different from that of the high-frequency part. The frequency parts are so far apart that the absorptivity of the middle part is not enough at 90%. As a increases, the high-frequency part gradually moves to the low-frequency part, and the overlap of the two parts makes the middle of the band rise to more than 90%, and if it continues to rise, the two parts overlap too much, making the bandwidth narrower. Figure 16(d) illustrates the change of PCR with a. It can be seen that when a is less than 154 μm, the bandwidth is gradually narrowed, and if a is greater than 154 μm, the absorption bandwidth will be lost, so it is appropriate to choose a = 144 μm. As mentioned earlier, the thickness variation of the dielectric layer can affect the S-parameters. In Fig. 16(e), with the increase of $t2$, the absorption band moves to the lower frequency as a whole, and the reasons for low frequency and high-frequency absorption are different. Therefore, the effect of $t2$ on the two parts is different, so the two parts are separated and the absorption band is

Optics EXPRESS

broken in the middle. In Fig. 16(f), the dotted line represents the dividing line where PCR is 90%, and the bandwidth and frequency do not change much. In pursuit of better performance within the working range, a dashed line marks the boundary where the PCR is 95%. It can be seen from the diagram that the relatively stable range of bandwidth is $t2$ = 29-33 μm, so it is more appropriate to choose $t2$ = 31 μm.

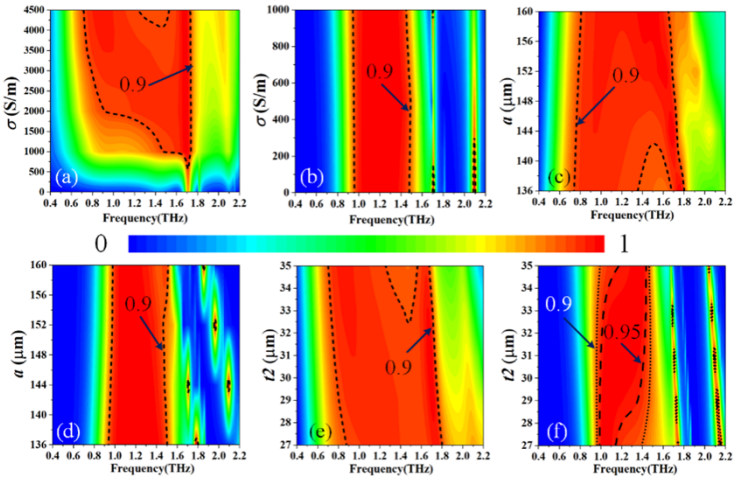

Fig. 16. The curves to investigate the influences of different variables. (a), (c), (e) The diagrams at absorption state of parameters σ, a, $t2$. (b), (d), (f) The diagrams at PC state of σ, a, $t2$.

3.3. *Polarization stability and incident angle*

For the performance of the device at different polarization angles, it can reflect the working effect of the device when it accepts incomplete horizontal or vertical incident waves. As shown in Fig. 17(a), the absorption bandwidth gradually decreases with the increase of the angle, and at θ=45° it reaches the narrowest, and then gradually restores the original bandwidth. The reasons for this phenomenon are: firstly, although the pattern on the top layer is a symmetrical shape, the difference between the copper arc and the silicon arc cannot be ignored. Secondly, the absorption bandwidth depends on the widening of the air resonator, and the main axis of the arrangement pattern of the cavities is a 4-fold symmetry axis, which cannot be restored after rotating 45°, which is an important reason for the change of the bandwidth. According to the principle of PC, the incident EMW can be polarized only if the components on the u-axis and the v-axis exist at the same time, and ideally, the components should be equal in size. Thus, as demonstrated in Fig. 17(b), when the polarization angle increases, the PCR decreases rapidly, all below 90% at deviations of 10°, and at 45° the PCR is 0 due to the absence of the component on the u-axis, which is consistent with the theory. Figure 17(c) displays the change in device performance with the increase of the incident angle. It can be seen that the absorption bandwidth is extremely sensitive to the angle, and the absorption band is interrupted in the range of more than 5°. In Fig. 17(d), also The breakpoint occurs when the incident angle is equal to 5°. This is because when the incident angle increases, for the incident wave, the original top layer parallel to the wavefront not only loses its symmetry but also changes from a two-dimensional surface to a three-dimensional structure, and it is difficult to meet the conditions of phase, impedance, and so on.

Optics EXPRESS

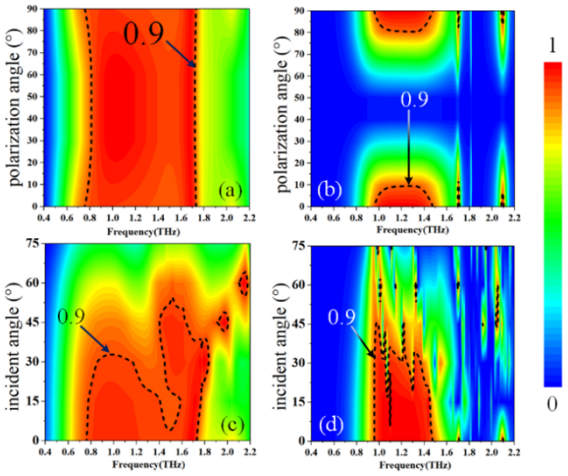

Fig. 17. (a)-(b) The performance under different polarization angles, (a) absorptivity, (b) PCR. (c)-(d) the performance under different polarization angles, (c) absorptivity, (d) PCR.

3.4. *Effective impedance*

The premise that the device can lose EMWs is that the EMWs can fully enter the device. Therefore, the mechanism of the device absorbing EMWs can be verified by checking whether the effective impedance of the device matches the free space. The formula for calculating effective impedance Z_{eff} can be written as [31]:

$$Z_{eff} = \frac{Z_0}{\frac{1-S_{11}}{1+S_{11}} - n_1 \frac{e^{(-jnk_0(h+n_0))} + e^{(jnk_0(h+n_0))}}{e^{(-jnk_0(h+n_0))} - e^{(jnk_0(h+n_0))}}} \tag{17}$$

In Eq. (17), S_{11} represents the reflection coefficient, and Z_0, n_0, and k_0 are the impedance, refractive index, and wave vector of free space, respectively. At the same time, since the device is required to achieve perfect absorption, the reflection coefficient should ideally be zero, and Eq. (17) can be simplified as:

$$Z_{eff} = \frac{Z_0}{1 - n_1 \frac{e^{(-jnk_0(h+n_0))} + e^{(jnk_0(h+n_0))}}{e^{(-jnk_0(h+n_0))} - e^{(jnk_0(h+n_0))}}} \tag{18}$$

According to the impedance matching theory, the relative impedance Z_r can be introduced to describe the degree of matching between the effective impedance and the impedance of the free space. Under ideal conditions, the real part of the Z_r is 1 and the imaginary part is 0. The expression of Z_r is as follows:

$$Z_r = \frac{Z_{eff}}{Z_0} = \sqrt{\frac{(1+S_{11})^2 - {S_{21}}^2}{(1-S_{11})^2 - {S_{21}}^2}} \tag{19}$$

As signified in Fig. 18, the actual part of the calculated effective impedance is slightly larger than 1, and the imaginary part is near 0. This is because the device cannot get to the ideal state and can only achieve more than 90% absorption. At the same time, it can be seen from the comparison of the four structures that, taking the effective impedance around 1.8 THz as an example, the peak value of the real part decreases from the initial value greater than 3.5 to less than 2.75, and the peak value of the imaginary part increases from close to −3 to above

Optics EXPRESS

−1.5. This indicates that as the structural optimization gradually expands the bandwidth, the real part of the corresponding effective impedance gradually converges to 1, and the imaginary part gradually converges to 0.

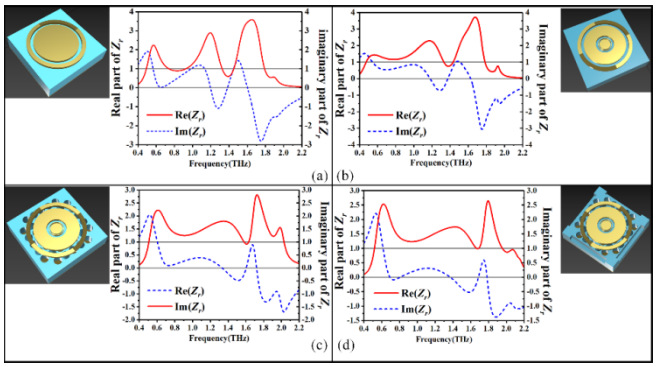

Fig. 18. The effective impedance of (a) structure 1, (b) structure 2, (c) structure 3, and (d) structure 5.

3.5. Simulation and manufacturing

All the above simulation results are obtained by the software HFSS, and the numerical method is the finite element method. The excitation of photocarriers in the silicon can be done by an optical pump beam. As mentioned in Ref. [35], with the help of the pump, the regulation of the conductivity between $1 \sim 1 \times 10^5$ S/m can be achieved, which obviously satisfies the needs of this paper. First, it is the preparation of silicon, polyimide, and copper films in the basic structure. A certain amount of 4, 4'-diaminodiphenyl ether was dissolved in an appropriate amount of N, N-dimethylacetamide, then a certain amount of pyromellitic dianhydride was added step by step, and the reaction was stirred at a constant speed for 2 h, and then aging for 24 hours, vacuumize, and finally pour the glue solution on the glass plate to coat the film. After laying the film, put it into an oven for gradient heating (80°C to 330°C), and take out the film after cooling it to room temperature [36]. There are many preparation methods for the copper films, such as magnetron sputtering, electron beam evaporation, electroplating, and so on. Considering the advantages of simple operation and no pollution, the copper base plate can be prepared by the following method: the unheated polyimide film is cleaned with acetone, then ion-cleaned and dried, and then used as the substrate, using the magnetron sputtering method of sputtering deposition of copper films with a thickness of 3 μm [37]. Amorphous silicon films can be deposited by plasma-enhanced chemical vapor deposition [38]. Second, the photoresist is coated on the copper and polyimide films, and all the structures can be realized by photolithography [39,40]. After that, the silicon and polyimide copper films are combined, and the pattern of the uppermost layer is formed again utilizing photolithography. Finally, the fabrication of copper arcs is achieved using electron beam lithography.

4. Conclusion

In this paper, a multifunctional device in the THz range has been designed. The device applies the photoconductivity effect of silicon to switch functions between absorption and PC by changing the conductivity of silicon through light. When the conductivity of silicon S is attained around 3500 S/m, it achieves an absorption band over 90% from 0.75 to 1.73 THz, with 0.98 THz absolute bandwidth and 79% RB. When the conductivity of silicon is close to 1 S/m, which means no illumination, the two copper arcs realized a PC band in the range of 0.96-1.47 THz,

Optics EXPRESS

with 0.51 THz absolute bandwidth and 42% RB. In addition, the mechanism of absorption and PC is investigated, and the influences of polarization angle, incident angle, and structural parameters through the current diagrams and data curves. The proposed device has promising use in communication, electromagnetic cloaking, THz modulation, and so on.

Funding. National College Student Innovation Training Program (202210293014Z).

Disclosures. The authors declare no conflicts of interest.

Data Availability. Data underlying the results presented in this paper are not publicly available at this time but may be obtained from the authors upon reasonable request.

References

1. D. R. Smith, J. B. Pendry, and M. C. K. Wiltshire, "Metamaterials and negative refractive index," Science **305**(5685), 788–792 (2004).
2. M. Wu, X. Zhao, J. Zhang, J. Schalch, and G. Duan, K. Cremin, R. D. Averitt, and X. Zhang, "A three-dimensional all-metal terahertz metamaterial perfect absorber," Appl. Phys. Lett. **111**(5), 051101 (2017).
3. V. V. Klimov, "Novel approach to a perfect lens," JETP Lett. **89**(5), 229–232 (2009).
4. D. Wen, F. Yue, G. Li, G. Zheng, K. Chan, S. Chen, M. Chen, K. Li, P. W. H. Wong, K. W. Cheah, E. Y. B. Pun, S. Zhang, and X. Chen, "Helicity multiplexed broadband metasurface holograms," Nat. Commun. **6**(1), 8241 (2015).
5. E. R. Brown, "Fundamentals of terrestrial millimeter-wave and THz remote sensing," Int. J. High Speed Electron. Syst. **13**(04), 995–1097 (2003).
6. P. Mookiah and K. R. Dandekar, "Metamaterial-substrate antenna array for MIMO communication system," IEEE Trans. Antennas Propag. **57**(10), 3283–3292 (2009).
7. Q. Ma and T. J. Cui, "Information metamaterials: bridging the physical world and digital world," PhotoniX **1**(1), 1–32 (2020).
8. W. Yang and Y. S. Lin, "Tunable metamaterial filter for optical communication in the terahertz frequency range," Opt. Express **28**(12), 17620–17629 (2020).
9. N. I. Landy, S. Sajuyigbe, J. J. Mock, D. R. Smith, and W. J. Padilla, "Perfect metamaterial absorber," Phys. Rev. Lett. **100**(20), 207402 (2008).
10. X. He, S. Yan, G. Lu, Q. Zhang, F. Wu, and J. Jiang, "An ultra-broadband polarization-independent perfect absorber for the solar spectrum," RSC Adv. **5**(76), 61955–61959 (2015).
11. B. X. Wang and G. Z. Wang, "Quad-band terahertz absorber based on dipolar resonances of metamaterial resonator," Plasmonics **13**(3), 1097–1103 (2018).
12. X. Jiang, S. Wang, and H. Wu, "Metamaterial Absorber with Tunable Absorption Bandwidth Based on Vanadium Dioxide," Acta Polym. Sin. **51**(1), 0151124 (2022).
13. Z. Xu, R. Gao, C. Ding, L. Wu, Y. Zhang, D. Xu, and J. Yao, "Photoexited switchable metamaterial absorber at terahertz frequencies," Opt. Commun. **344**, 125–128 (2015).
14. Y. Z. Cheng, W. Withayachumnankul, A. Upadhyay, D. Headland, Y. Nie, R. Z. Gong, M. Bhaskaran, S. Sriram, and D. Abbott, "Ultrabroadband reflective polarization convertor for terahertz waves," Appl. Phys. Lett. **105**(18), 181111 (2014).
15. J. Asada and S. Nishiwaki, "Optical element converting linear polarization into circular-tangential polarization," Appl. Opt. **34**(22), 4768–4771 (1995).
16. X. Yu, X. Gao, W. Qiao, L. Wen, and W. Yang, "Broadband tunable polarization converter realized by graphene-based metamaterial," IEEE Photonics Technol. Lett. **28**(21), 2399–2402 (2016).
17. X. Gao, W. L. Yang, H. F. Ma, Q. Cheng, X. H. Yu, and T. J. Cui, "A reconfigurable broadband polarization converter based on an active metasurface," IEEE Trans. Antennas Propag. **66**(11), 6086–6095 (2018).
18. M. Barkabian, N. Sharifi, and N. Granpayeh, "Multi-functional high-efficiency reflective polarization converter based on an ultra-thin graphene metasurface in the THz band," Opt. Express **29**(13), 20160–20174 (2021).
19. F. Ding, S. Zhong, and S. I. Bozhevolnyi, "Vanadium dioxide integrated metasurfaces with switchable functionalities at terahertz frequencies," Adv. Opt. Mater. **6**(9), 1701204 (2018).
20. M. Kafesaki, N. H. Shen, S. Tzortzakis, and C. M. Soukoulis, "Optically switchable and tunable terahertz metamaterials through photoconductivity," J. Opt. **14**(11), 114008 (2012).
21. C. Huang, C. Zhang, J. Yang, B. Sun, B. Zhao, and X. Luo, "Reconfigurable metasurface for multifunctional control of electromagnetic waves," Adv. Opt. Mater. **5**(22), 1700485 (2017).
22. L. Zeng, H. F. Zhang, G. B. Liu, and T. Huang, "A three-dimensional Linear-to-Circular polarization converter tailored by the gravity field," Plasmonics **14**(6), 1347–1355 (2019).
23. J. Xu, R. Yang, Y. Fan, Q. Fu, and F. Zhang, "A review of tunable electromagnetic metamaterials with anisotropic liquid crystals," Front. Phys. **9**, 633104 (2021).
24. Z. M. Liu, E. D. Gao, Z. B. Zhang, H. J. Li, H. Xu, X. Zhang, X. Luo, and F. Q. Zhou, "Dualmode on-to-off modulation of plasmon-induced transparency and coupling effect in patterned graphene-based terahertz metasurface," Nanoscale Res Lett **15**(1), 1–13 (2020).
25. Y. Cheng, J. Liu, F. Chen, H. Luo, and X. Li, "Optically switchable broadband metasurface absorber based on square ring shaped photoconductive silicon for terahertz waves," Phys. Lett. A **402**, 127345 (2021).

Optics EXPRESS

26. Z. Song, Z. Wang, and M. Wei, "Broadband tunable absorber for terahertz waves based on isotropic silicon metasurfaces," Mater. Lett. **234**, 138–141 (2019).
27. X. Zhao, Y. Wang, J. Schalch, G. Duan, K. Cremin, J. Zhang, C. Chen, R. D. Averitt, and X. Zhang, "Optically modulated ultra-broadband all-silicon metamaterial terahertz absorbers," ACS Photonics **6**(4), 830–837 (2019).
28. J. Li, C. Zheng, G. Wang, J. Li, H. Zhao, Y. Yang, Z. Zhang, M. Yang, L. Wu, J. Li, Y. T. Zhang, Y. Zhang, and J. Q. Yao, "Circular dichroism-like response of terahertz wave caused by phase manipulation via all-silicon metasurface," Photonics Res. **9**(4), 567–573 (2021).
29. O. Ayop, M. K. A. Rahim, N. A. Murad, and H. A. Majid, "Metamaterial absorber based on circular ring structure with and without copper lines," Appl. Phys. A **117**(2), 651–656 (2014).
30. A. S. Dhillon, D. Mittal, and E. Sidhu, "THz rectangular microstrip patch antenna employing polyimide substrate for video rate imaging and homeland defence applications," Optik **144**, 634–641 (2017).
31. D. R. Smith, D. C. Vier, T. Koschny, and C. M. Soukoulis, "Electromagnetic parameter retrieval from inhomogeneous metamaterials," Phys. Rev. E **71**(3), 036617 (2005).
32. S. Zhuang, X. Li, T. Yang, L. Sun, O. Kosareva, C. Gong, and W. Liu, "Graphene-Based Absorption–Transmission Multi-Functional Tunable THz Metamaterials," Micromachines **13**(8), 1239 (2022).
33. Y. Qiu, D. X. Yan, Q. Y. Feng, X. J. Li, L. Zhang, G. H. Qiu, and J. N. Li, "Vanadium dioxide-assisted switchable multifunctional metamaterial structure," Opt. Express **30**(15), 26544–26556 (2022).
34. M. S. U. Afsar, M. R. I. Faruque, M. B. Hossain, A. M. Siddiky, M. U. Khandaker, A. Alqahtani, and D. A. Bradley, "A New Octagonal Close Ring Resonator Based Dumbbell-Shaped Tuning Fork Perfect Metamaterial Absorber for C- and Ku-Band Applications," Micromachines **13**(2), 162 (2022).
35. N. H. Shen, M. Massaouti, M. Gokkavas, J. M. Manceau, E. Ozbay, M. Kafesaki, T. Koschny, S. Tzortzakis, and C. M. Soukoulis, "Optically implemented broadband blueshift switch in the terahertz regime," Phys. Rev. Lett. **106**(3), 037403 (2011).
36. L. Liu, H. Shi, L. Weng, J. Ding, and W. Cui, "The effects of particle size on the morphology and properties of polyimide/nano-Al2O3 composite films," Polym. Polym. Compos. **22**(2), 117–122 (2014).
37. J. F. Piersona, D. Wiederkehra, and A. Billardb, "Reactive magnetron sputtering of copper, silver, and gold," Thin Solid Films **478**(1-2), 196–205 (2005).
38. Y. He, C. Yin, G. Cheng, L. Wang, and X. Liu, "The structure and properties of nanosize crystalline silicon films," J. Appl. Phys. **75**(2), 797–803 (1994).
39. P. Molet, J. L. Garcia-Pomar, C. Matricardi, M. Garriga, M. I. Alonso, and A. Mihi, "Ultrathin Semiconductor Superabsorbers from the Visible to the Near-Infrared," Adv. Mater. **30**(9), 1705876 (2018).
40. Y. M. Yang, I. I. Kravchenko, D. P. Briggs, and J. Valentine, "All-dielectric metasurface analogue of electromagnetically induced transparency," Nat. Commun. **5**(1), 5753 (2014).